Use of Nanostructured Alumina Thin Films in Multilayer Anti-Reflective Coatings

Jarno Reuna[a,1], Arto Aho[a], Riku Isoaho[a], Marianna Raappana[a], Timo Aho[a], Elina Anttola[a], Arttu Hietalahti[a], Antti Tukiainen[a], Mircea Guina[a]

[a] *Optoelectronics Research Centre, Physics Unit, Faculty of Engineering and Natural Sciences, Tampere University, P.O. Box 692, FIN-33014 Tampere, Finland*

[1]*Corresponding author:* jarno.reuna@tuni.fi

Keywords: De-Ionized Water, Thin film coatings, Porosity, Aluminum Oxide, Multilayer

Abstract

A new method for modification of planar multilayer structures to create nanostructured aluminum oxide anti-reflection coatings is reported. The method is non-toxic and low-cost, being based on treatment of the coating with heated de-ionized water after the deposition of aluminum oxide. The results show that the method provides a viable alternative for attaining a low reflectance ARC. In particular, a low average reflectivity of ~3.3 % is demonstrated in a broadband spectrum extending from 400 nm to 2000 nm for ARCs deposited on GaInP solar-cells, the typical material used as top-junction in solar cell tandem architectures. Moreover, the process is compatible with volume manufacturing technologies used in photovoltaics, such as ion beam sputtering and electron beam evaporation.

1. Introduction

Aluminum oxide (Al_2O_3) is a versatile non-toxic low refractive index insulator widely used in optical coatings[1,2] and passivation layers[3–5]. It can be deposited by a wide range of thin film technologies, including electron-beam (e-beam) evaporation[6], ion beam sputtering (IBS)[7], plasma-enhanced chemical deposition (PECVD)[8], atomic layer deposition (ALD)[5,9], pulsed laser deposition (PLD)[2], radiofrequency (RF)[10] and direct current (DC)[11] sputtering. Alumina is known to be an amphoteric substance[12] and to form porous structures via anodic growth[13,14] and sol-gel

processes[15,16]. These material properties could be utilized in controlled corrosion process to fabricate nanoporous Al_2O_3 thin film with anti-reflective functionalities.

Porous nanostructures have successfully been utilized in advanced solar cell anti-reflective coatings (ARC), where they have enabled broadband operation and very low average reflectivity[17,18]. Many of these nanostructures have exploited bio-mimicked concepts, i.e. moth-eye structures fabricated by nanoimprinting lithography[18,19], but also lithography free methods have been developed[20,21]. The lithography free processes offer more streamlined manufacturing when compared to multi-step lithography methods. In addition to the low average reflectance, the nanostructures can offer longer optical paths within the solar cell by enhancing the surface scattering, which results in better absorption of light in the solar cell junctions and increases the total conversion efficiency[19,22]. Combining a nanoporous top layer with traditionally used multilayer (ML) ARC for III–V solar cells could offer even better performance over broader spectral window[23,24]; yet in terms of making this a feasible approach for wider use one would like to avoid multi-step post-coating processing.

Recent studies have shown that amorphous thin film Al_2O_3 forms porous structure when treated with heated de-ionized water (DIW) [10,25]. Kauppinen *et al.* [25] have studied and developed a process to utilize the instability of ALD deposited alumina with DIW to fabricate porous anti-reflective coating for glass and black silicon solar cells. Additionally, Dokmai *et al.*[10] have studied RF sputtered alumina films taking a closer look to the process mechanism of alumina corrosion in DIW. A potentially interesting possibility is also to use DIW-induced processes for fabrication of porous Al_2O_3 nanostructure using deposition techniques routinely employed in fabrication of multilayer broadband ARCs, namely e-beam and IBS. Benefits of these commonly used deposition methods include fast coating cycles, relatively fast growth rates (0.2-2 μm/h) and ability to use several different materials in one deposition run, which enables single-run deposition of the suggested ML ARC.

To this end, we demonstrate the formation of porous nanostructured alumina fabricated by the DIW driven process and integrated as a topmost layer of a planar multilayer ARC deposited by e-beam and IBS. By combining alumina with materials typically used for planar ARCs, such as titanium dioxide (TiO_2), having a relatively high refractive index enables maximizing the ARC functionality over a wider spectrum. Such broadband ARC structures are especially needed for

high efficiency III–V multijunction solar cells[26] where a cost effective and volume reproducible technology for coating deposition is a must.

2. Methods

Purpose of any ML ARC is to form a destructive set of interference that cancels out any reflections induced by the coated structure and to minimize the refractive index difference between the surrounding media (usually air) and the last layer of the thin film stack. Here we have used transfer matrix method (TMM)[27–29] to design and simulate both the traditional planar ML structure and the nanostructured Al_2O_3 layer on top of it, as well as to model the III–V solar cell beneath the coating.

E-beam Al_2O_3 was evaporated using a custom-built evaporator by Instrumentti Mattila Oy; the system includes an electron source, a crucible, sweep controls from Telemark Ltd, and a quartz monitoring from Intellemetrics Global Ltd. The system base pressure prior to evaporation is approximately 1×10^{-5} mbar and the electron beam is formed with Telemark's 7-1/2 turn tungsten filament. The deposition temperature was 150 °C, as measured from the backside of the steel substrate holder, where the holder temperature is approximated to be in thermal equilibrium with the substrate during the thin film deposition. The measurement utilized a K-type thermocouple for temperature monitoring and the heating of the substrates was done radiatively by halogen lamps. As evaporation material we used Al_2O_3 granules with the size of 1.5-4 mm and with a purity of 99.99 %. Evaporation parameters for all used oxides are given in the Appendix A.

IBS alumina was deposited with Navigator 700 sputtering system (Cutting Edge Coatings GmbH). Sputtering was done using $Ar{:}O_2$ gas mixture with a flow ratio of 8:5 sccm ensuring a reactive O_2 atmosphere with a pressure of 4.5×10^{-4} mbar. A 200 × 200 mm aluminum plate with purity of 99.999 % was used as the target. Sputtering voltage was 1.26 kV and the RF power of the ion source was 102 W. During the deposition, the sample holder was rotated at 60 rpm to guarantee uniform deposition. The thickness was controlled via *in-situ* broadband optical monitoring, which measures the transmittance of a transparent monitoring substrate and fits the measurement data to the theoretical spectrum calculated with the refractive indices and extinction coefficients of the given materials. The sputtering parameters for all oxides used are given in the Appendix A.

The DIW used in the treatment had a resistivity of 18.4 MΩ and was kept in glass beakers pre-heated to temperature of 90 °C on a hotplate before sample immersion. The temperature of the

solution was constantly monitored during the treatment and no agitation was used. Treatment time was kept constant at 30 minutes. Several characterization samples for DIW treatment were deposited on silicon (Si) wafer pieces, without removing the native oxide[30] from the substrate.

The film thicknesses and refractive indices of the dielectric layers were determined with a Rudolph AutoEL III Null ellipsometer equipped with a He/Ne laser at $\lambda = 632.8$ nm. As parameters for ellipsometric calculations we used a refractive index of Si-substrate $n_S = 3.863$, a substrate extinction coefficient $k_S = 0.162$, and an angle of incidence of 70°. The refractive indices and film thicknesses in this study are average values of several measurements. The error limits have been calculated for 95 % level of confidence and then added the precision of the ellipsometer (refractive index 0.001, thickness 1 Å). For refractive index this gives an error limit of ±0.002 and for thickness an error limit of ±2 Å.

Scanning electron microscope (SEM) images were taken with a ΣIGMA™ FESEM operated with SmartSEM® software, both products of Carl Zeiss NTS Ltd. Acceleration voltage was 1 kV and the aperture size was 10 µm. For surface roughness measurements we used a Dimension™ 3100 Atomic force microscope (AFM) from Veeco Ltd and the image data was constructed with WSxM 5.0 Develop 8.2 software [31]. For grazing incidence x-ray diffraction (GIXRD) measurements a PANalytical X'Pert³ MRD system was used.

For the transmission and the reflectance measurements of the deposited thin films we used a PerkinElmer Lambda 1050 UV/VIS/NIR spectrophotometer. Reflectance was measured at 8° angle of incidence, which is the smallest measurable angle when using the universal reflectance accessory module. The transmittance was measured with normal angle of incidence by using Scan Lambda 1050 transmittance module. The measured data was also used for simulations and fitting of the optical properties of the alumina, which was done with *Essential Macleod*© thin film software, that calculates the structures using TMM. Figure 1 shows the starting point for our approximation of the reflectivity of the porous Al_2O_3 and how the optical properties can be calculated by transforming the structure to very thin finite layers of varying refractive index, so called rugate design. In the model, n_m is the refractive index of the film material and n_i is the refractive index of the incident medium.

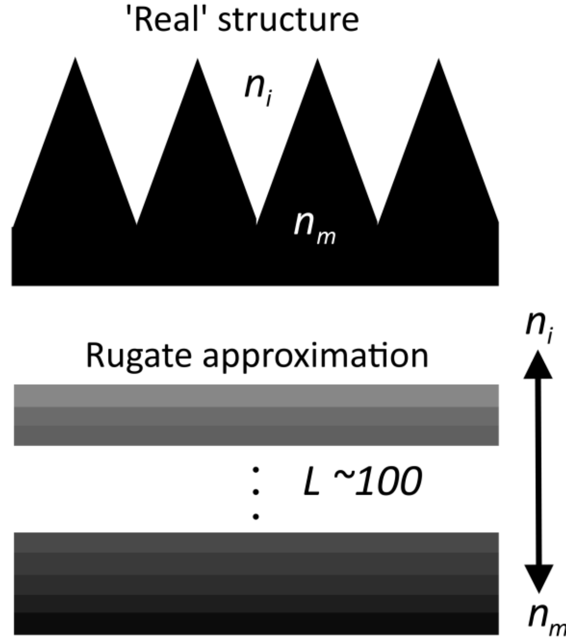

Fig. 1. *Rugate filter principle for fitting optical properties of porous* Al_2O_3 *films.*

In the rugate design we vary the packing density of the film material of each individual layer (L), which in turn scales the refractive index according to the Maxwell-Garnett approximations[32,33]. The simulation for the packing density of each layer follows the equation:

$$\rho_L = 1 - (1 - (N - L)/N) \,, \tag{1}$$

where ρ_L is the packing density of the current layer, N is the total number of layers and L is the current layer number. The refractive index of each layer is calculated with the equation:

$$n_L = \rho \cdot n_m \,, \tag{2}$$

where n_L is the refractive index of an individual layer and n_m is the refractive index of the film material. For the simulations we started with 100 layers with the total thickness of the stack being 0.25 quarter wavelength of optical thickness at the wavelength of 633 nm. Then we used the Simplex© algorithm provided by the software to match the functionality of the stack to the spectrophotometer measurements by altering the physical thicknesses of the layers. The starting designs and fitted rugate layer values for the nanostructured alumina are given in the Appendix B.

Finally, when it comes to methodology, we should mention that the ARC performance of the film was tested on single-junction n-on-p GaInP solar cells, which were grown by molecular beam epitaxy on GaAs substrates using a Veeco GEN20 MBE system.

3. Results

To be able to process the ARC with DIW treatment, we needed to make sure that the other material components regularly used in optical coatings by e-beam and IBS would not be as prone to morphological changes as the alumina. Good measure of the film properties before and after DIW treatment is gained by ellipsometry that gives both thickness and refractive index of the film. The ellipsometry results for different e-beam and IBS oxides are shown in Table 1.

Table 1 *Ellipsometry results for the oxides analyzed before and after DIW treatment. Refractive indices ±0.002 and thicknesses ±2 Å with 95 % level of confidence.*

		Material	Before DIW	After DIW	Difference [%]
IBS	n (@633nm)	Al_2O_3	1.671	N/A	N/A
	Thick. [Å]		1217	N/A	N/A
		SiO_2	1.483	1.481	-0.2
			1025	1014	-1.1
		TiO_2	2.372	2.370	-0.1
			1046	1043	-0.3
		Ta_2O_5	2.110	2.109	-0.1
			743	740	-0.4
E-beam	n (@633nm)	Al_2O_3	1.583	N/A	N/A
	Thick. [Å]		1245	N/A	N/A
		SiO_2	1.449	1.444	-0.3
			907	875	-3.5
		TiO_2	2.177	2.170	-0.3
			514	510	-0.7
		Ta_2O_5	1.948	1.930	-0.9
			632	630	-0.3

For Al_2O_3 we were unable to calculate the refractive index and thickness of the films after the DIW treatment. With monochromatic ellipsometry this can mean inhomogeneous layer structure, which

indicates that some morphological changes took place for alumina films during DIW immersion. Other tested oxide materials showed little to no change in film properties due to the treatment.
To verify what happened to the alumina films during DIW treatment, we imaged the samples with SEM and compared the film morphologies before and after the DIW processing. Figure 2 shows SEM surface images of untreated and DIW-treated Al_2O_3 for both e-beam and IBS deposited films.

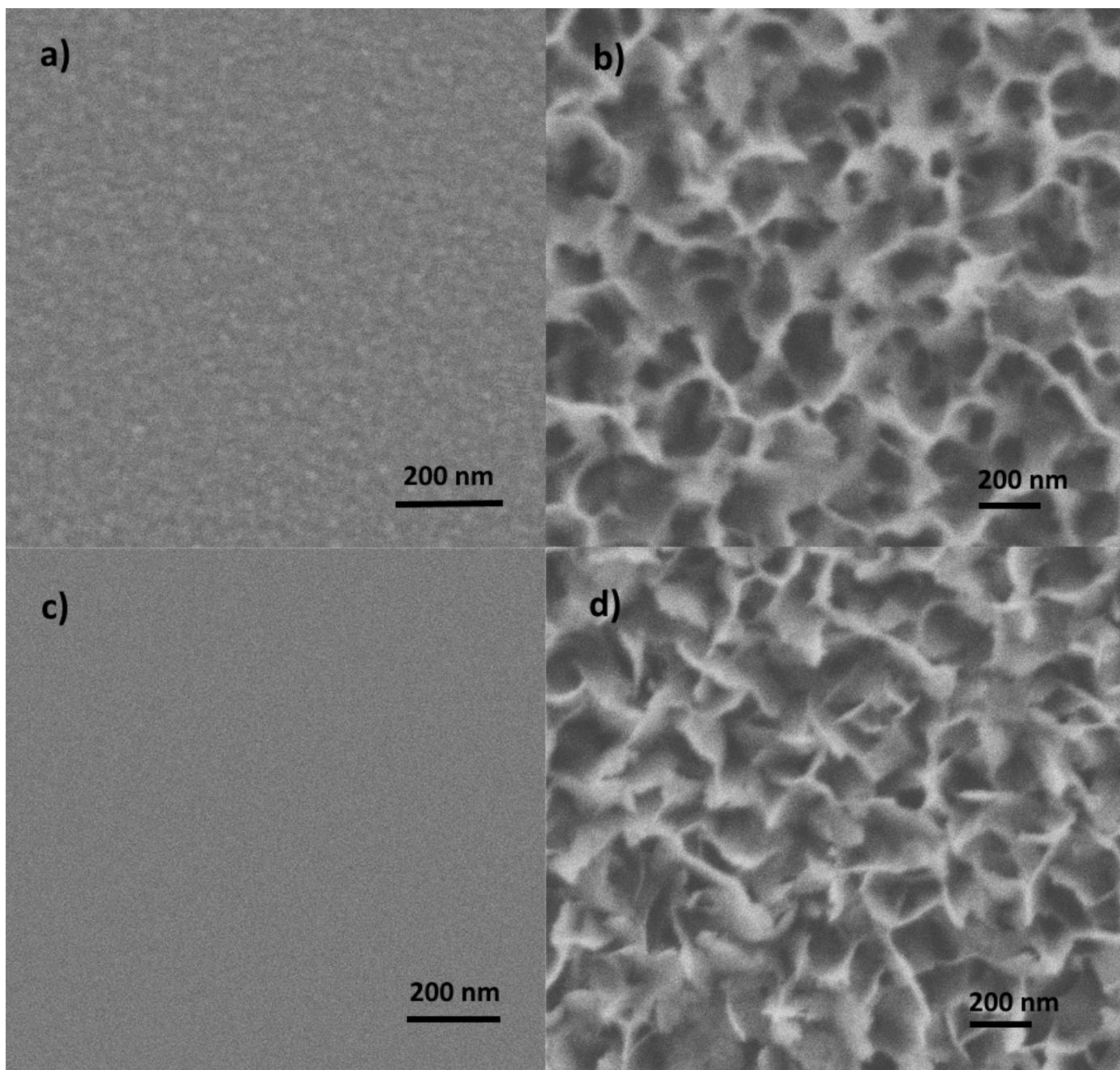

Fig. 2. *SEM surface images of e-beam evaporated Al_2O_3 before (a) and after (b) DIW treatment and IBS deposited Al_2O_3 before (c) and after (d) DIW treatment.*

From the SEM images we can see that both Al_2O_3 layers, independent of the deposition method, are relatively smooth prior to DIW immersion and after the treatment they form a porous, almost

flower-like, structure. In the case of ALD grown Al_2O_3, it is hypothesized by Correa *et al.*[34] that the structural changes are due to the amorphous alumina hydrolyzing into aluminum hydroxides, namely β-$Al(OH)_3$ (bayerite) and α-$Al(OH)_3$ (gibbsite)[35,36]. According to their studies surface roughening and thickness change of the DIW treated samples matches to those of gibbsite and bayerite [37,38]. To confirm the possible crystallinity of the Al_2O_3 films, the IBS Al_2O_3 samples were measured with XRD before and after DIW treatment. The XRD scans revealed no crystalline orientation, strongly indicating that both the as deposited and DIW treated films are of amorphous nature. This hydrolysis of amorphous alumina causing the morphology changes is examined in more detail by Dokmai *et al.*[10].

To get a better sense of the height and roughness distribution of our samples, we used AFM scanning to measure the surface morphology, as shown in Figure 3.

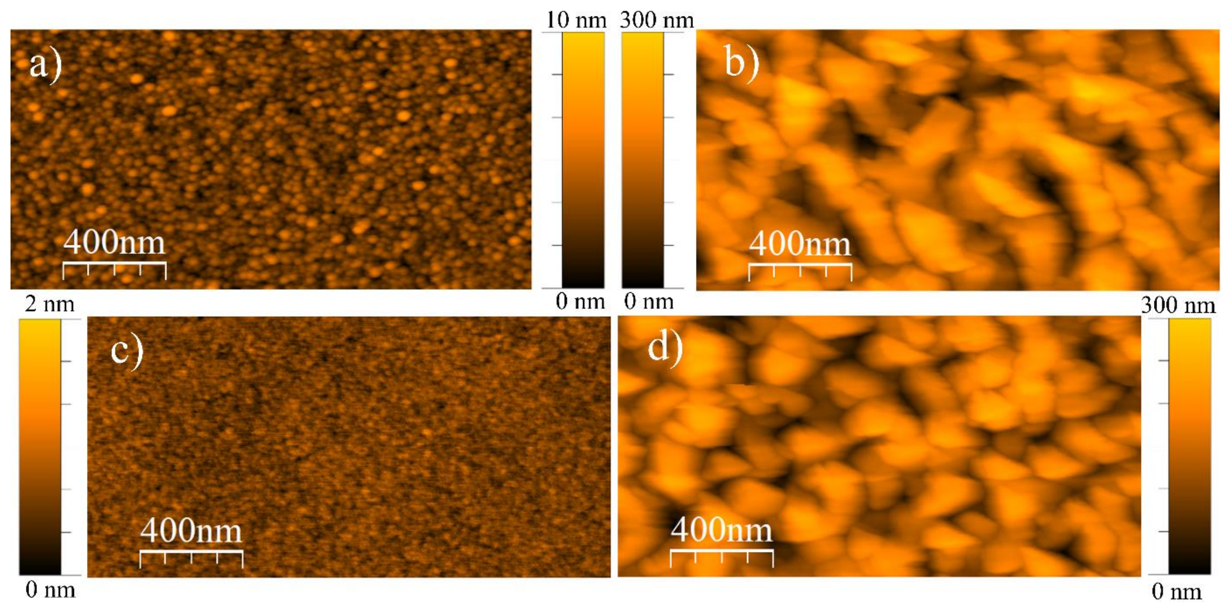

Fig. 3. *Surface topography of e-beam evaporated Al_2O_3 before (a) and after (b) DIW treatment and IBS deposited Al_2O_3 before (c) and after (d) DIW treatment measured with AFM.*

The AFM surface scans reveal a small difference in the height distribution of the pores of DIW treated samples in between the e-beam and IBS deposited films. We assume this to be related to the difference of the film quality in the as-deposited films, as the e-beam Al_2O_3 is slightly porous to begin with, whereas the IBS films are dense. Table 2 lists the numerical values for the surface

roughness and feature height and gives a nominal height difference of roughly 30 nm between the e-beam and IBS deposited Al_2O_3 after the DIW processing.

Table 2 *Surface roughness of the Al_2O_3 films before and after DIW treatment measured by AFM.*

	E-Beam		**IBS**	
	Untreated	**DIW**	**Untreated**	**DIW**
R_{rms} [nm]	0.86	41.09	0.13	42.10
R_{ave} [nm]	0.68	33.01	0.10	34.54
Average height [nm]	2.69	161.83	0.68	135.20
Max height [nm]	7.55	303.35	1.36	257.99

To verify the accuracy of the height distribution measured by AFM, we used SEM for cross-sectional imaging of the DIW treated IBS alumina. Figure 4 shows the corresponding heights of several alumina peaks.

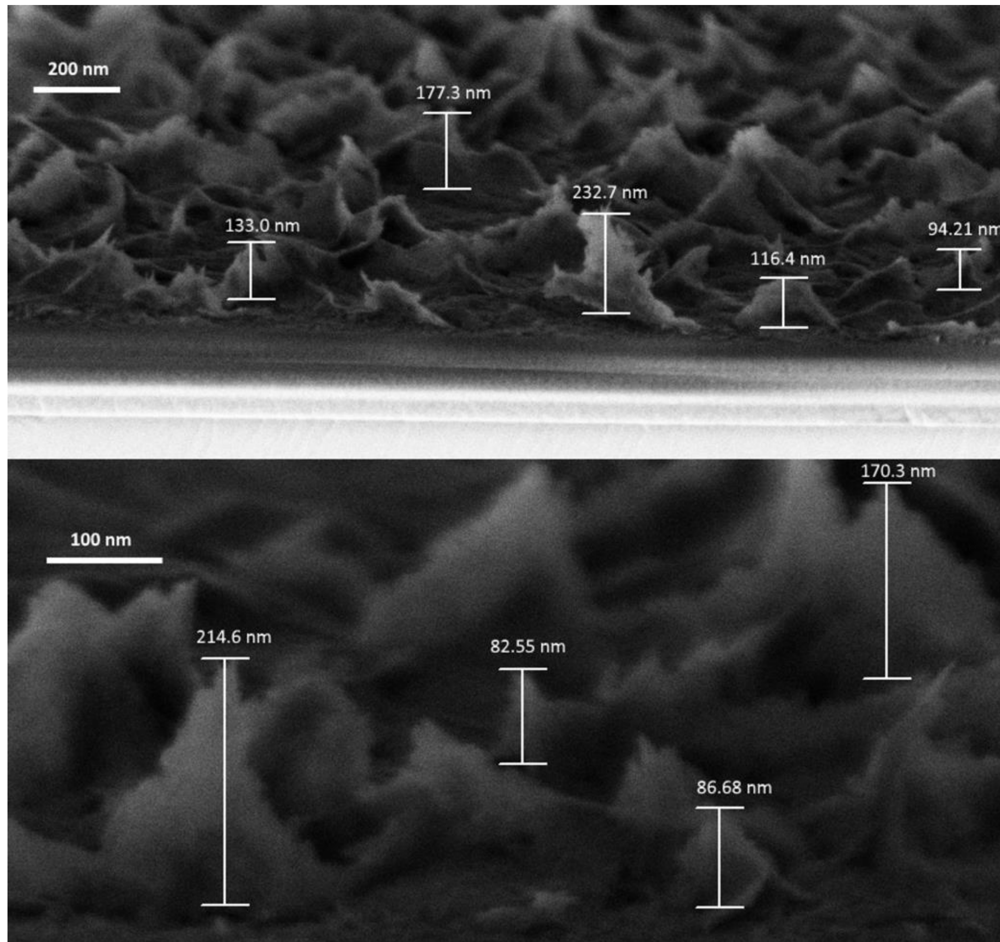

Fig. 4. *Cross-sectional SEM images of DIW treated IBS Al_2O_3 with measured heights for chosen sampling of the peaks.*

As already seen in Figure 2, Figure 4 shows the irregular morphology of the DIW treated Al_2O_3 and that the peak heights vary over 100 nm in length. The numerical data is well in line with the AFM measurements shown in Table 2.

Mechanical stability is an important issue for anti-reflection coatings in general and especially for porous coating types. However, we see that the mechanical durability is more connected to the environmental stability of the coating applications and not within the scope of this particular manuscript. Traditional Scotch tape test showed no signs of mechanical cracking or off-peeling of the coating under inspection of optical microscope, thus proving the mechanical stability sufficient for intended applications. In addition to the mechanical stability, the coating should remain clean enough to still function as an ARC. Any accumulating dust or moist on the nanostructured surface will likely reduce the transmission of the ARC and increase total losses. This can be solved by

very recently published fluoropolymerization process that makes the nanostructured alumina superhydrophobic[39]. Our specific aim is utilization of this ARC on the III-V multi-junction solar cell architectures, where for example the space solar cells are encapsulated with cover glass/plastic [40] and concentrated photovoltaics behind the concentration optics[41]. Therefore, the suggested coating could be taken in use as is.

To test and see how the IBS and e-beam deposited porous alumina can be utilized for ARCs, we deposited a single layer of Al_2O_3 on fused silica (FS) substrates with post-deposition DIW treatment and measured the spectral performance of these filters. The measured transmittances are shown in Figure 5.

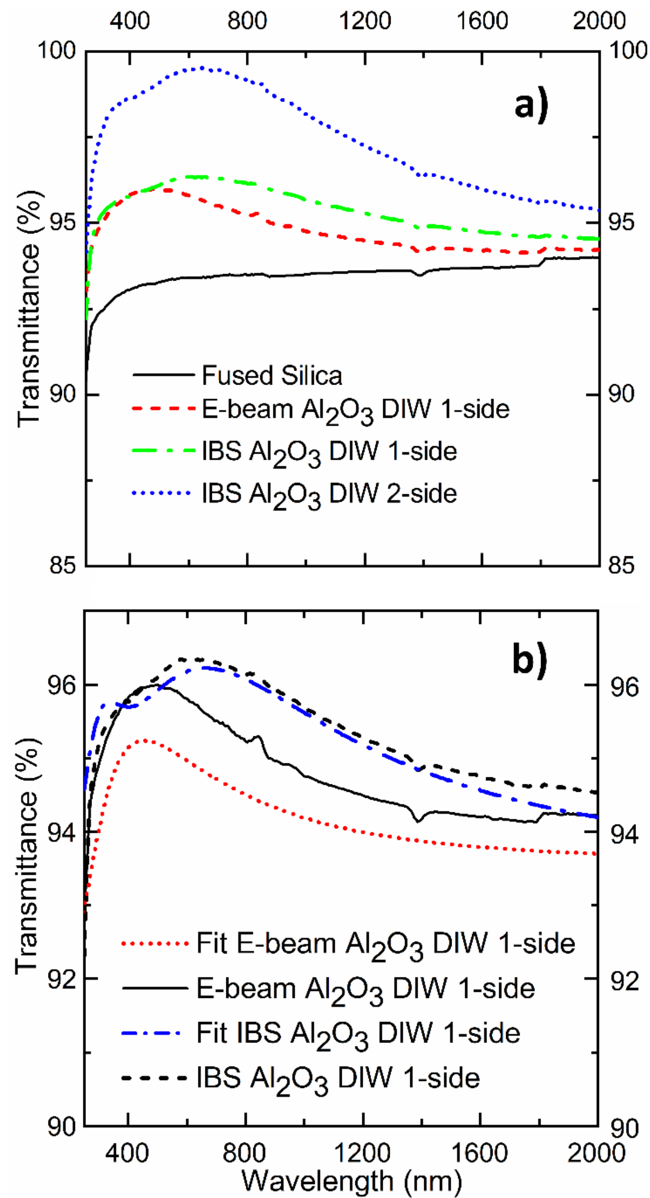

Fig. 5. *a) The transmission spectra for samples coated with porous Al_2O_3 films with the transmittance of a bare fused silica substrate. b) Rugate filter numerical fittings compared to the measured transmittance of the DIW treated alumina structures.*

For the one side coated DIW treated Al_2O_3 filters, the transmission is on average almost 95 % for both e-beam and IBS materials. The peak transmission wavelength of the filters differs slightly, pointing towards smaller feature size for e-beam deposited porous alumina than for the IBS deposited alumina. Based on the SEM and AFM comparison it would mean that the e-beam Al_2O_3 forms slightly narrower and taller build-ups than the IBS alumina. This also slightly reduces its

functionality as a graded index layer when compared to the IBS Al_2O_3, as can be seen in the difference of the transmission curves between 1-side coated filters. To neglect the effect of substrate backside reflectance, we also tested two side IBS porous alumina coated FS, which reached an impressive 99.5 % peak transmittance at λ = 600 nm and overall transmittance over 95.5 % spanning the wide spectral region of 300-2000 nm.

To be able to effectively design coatings for new applications utilizing porous alumina films, it would be beneficial to simulate the effects of the films when combined with other materials before the actual deposition. For this purpose, we used the rugate filter approximation and matched its performance to the measured reflectance of TiO_2/porous Al_2O_3 structures on silicon. To determine the applicability of the fit we used the alumina part of the fitting for comparison to the transmission measurements on FS as shown in Figure 5. b). For IBS deposited Al_2O_3 the fit works really well and only minor differences can be seen in the near ultraviolet and infrared parts of the spectrum. For e-beam deposited Al_2O_3 the fit is not nearly as good, as there is almost constant 1 % difference between the simulated and measured transmission of the film. However, even the e-beam simulation shows accurately the position of the peak transmission and the overall trend of the spectrum, which would make it useful for preliminary estimation of design functionalities.

As such, the used Si and FS substrates are a good starting point for material characterization, but as a part of an ARC on a real functional III–V solar cell (SC) the coatings might behave differently. Complex layer structure of the SC is also more challenging to simulate accurately for the preliminary optical designing of the ARC compared to a bare substrate. As the differences in functionality between e-beam and IBS deposited DIW treated alumina slightly favor the IBS deposited film, further ARC tests were done with IBS materials. The quality difference shown in this work is more related to the system specific limitations at our site than to the deposition methods itself, so no further comparison was made. To test out our nanoporous ARC structure and the accuracy of the used rugate model, we fabricated the DIW treated TiO_2/Al_2O_3 ARC by IBS on top of GaInP single-junction solar cell and simulated the entire structure to see the effectiveness of the model. GaInP SC is typically applied as the topmost junction in MJSC devices[42,43] and is thus a reasonable choice for ARC characterization sample. The comparison between simulation and spectrophotometer measurements is shown in Figure 6. a).

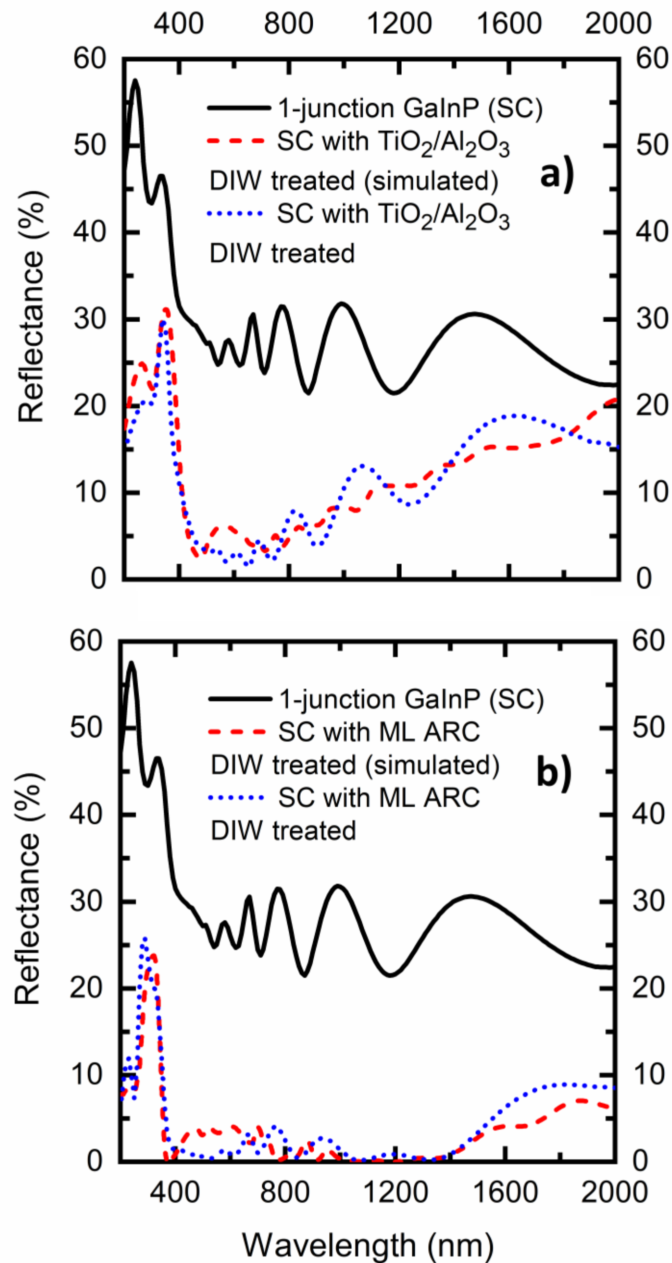

Fig. 6. *Real and simulated reflectance of GaInP single-junction SC with DIW treated TiO_2/Al_2O_3 ARC in a) and with an advanced multilayer ARC structure with the nanoporous Al_2O_3 in b).*

As Figure 6 shows, the simulated performance matches well to the actual measured reflectance of the coated GaInP solar cell and therefore the model is able to provide preliminary estimations of different ARC structures with the nanoporous Al_2O_3 top layer. The actual performance of the TiO_2/nanostructured Al_2O_3 ARC is not yet suitable to claim broadband operation nor does it reach

near 0 % reflectance at any point, so the design needs to be improved. To that end, we simulated and fabricated a ML ARC on top of the GaInP SC that combined all the tested IBS materials from Table 1. The reflectance of the ML ARC is plotted in the Figure 6 b). The ML ARC provides average reflectance of 3.28 % over a broadband spectral range from 400 to 2000 nm, which is especially beneficial for multijunction SC requiring such broadband operation. Regional average reflectance from 400 nm to 1000 nm is 1.65 % and from 1000 nm to 1500 nm the coating results in very impressive 0.86 % average reflectance. When comparing to the average reflectance of 2.7 % of a moth-eye patterned ARC[44], in the spectral range of 450 – 1650 nm, our approach provides almost 1 % lower average reflectance of 1.83 %. For multijunction solar cells the starting point for simulation and design is nominally different, but with the rugate filter approximation we can now have close estimations about the spectral performance for ARCs employing nanostructured Al_2O_3.

4. Conclusions

DIW based corrosion process for Al_2O_3 thin films was used to fabricate nanoporous optical coatings. The process does not alter the common hard coating oxides (SiO_2, TiO_2, Ta_2O_5) typically used in multilayer ARCs, which enables using the porous Al_2O_3 as a graded index layer on top of a multilayer ARC made of these oxides. The study showed that the post-deposition DIW treatment is compatible with both IBS and e-beam deposition methods, thus being applicable for a wide range of Al_2O_3 based ARCs. The optical effect of the topmost layer of the porous alumina can be simulated using a fitted rugate filter design, which then can be used to estimate the functionality of multilayer structures with TMM calculations. The performance of the nanoporous Al_2O_3 based ARCs was tested by fabricating such films on top of GaInP single-junction solar cells. The simulation model based on TMM rugate approach was also validated by fitting simulation and experimental results. The ML ARC exhibited a low average reflectance of ~3.3 % over a very broadband spectrum from 400 nm to 2000 nm, which is especially important in photovoltaic applications, where for example cover glasses, concentration lenses and other imperfect coated surfaces cause reflection losses.

The DIW corrosion based process for ML ARC with nanostructured Al_2O_3 is practical and can be easily implemented in efficient designs of ML coatings, we deem this development particular appealing for large scale exploitation in the next-generation SCs.

Acknowledgements

This work made use of Tampere Microscopy Center facilities at Tampere University. The authors acknowledge financial support provided by the European Research Council (ERC AdG AMETIST, #695116); the work is also part of the Academy of Finland PREIN flagship project (Grant No. 320165).

References

[1] D. Ristau and T. Gross, Adv. Opt. Thin Film. II **5963**, 596313 (2005).

[2] J. Gottmann and E.W. Kreutz, Surf. Coatings Technol. **116–119**, 1189 (1999).

[3] R. Watanabe, M. Kawashima, and Y. Saito, Thin Solid Films **590**, 98 (2015).

[4] K. Horiuchi, K. Nakada, S. Uchino, S. Hashii, A. Hashimoto, N. Aoki, Y. Ochiai, and M. Shimizu, Appl. Phys. Lett. **81**, 1911 (2002).

[5] L.H. Kim, K. Kim, S. Park, Y.J. Jeong, H. Kim, D.S. Chung, S.H. Kim, and C.E. Park, ACS Appl. Mater. Interfaces **6**, 6731 (2014).

[6] T.S. Eriksson, A. Hjortsberg, G.A. Niklasson, and C.G. Granqvist, Appl. Opt. **20**, 2742 (1981).

[7] J. Kischkat, S. Peters, B. Gruska, M. Semtsiv, M. Chashnikova, M. Klinkmüller, O. Fedosenko, S. Machulik, A. Aleksandrova, G. Monastyrskyi, Y. Flores, and W. Ted Masselink, Appl. Opt. **51**, 6789 (2012).

[8] C.E. Chryssou and C.W. Pitt, Appl. Phys. A Mater. Sci. Process. **65**, 469 (1997).

[9] A.I. Abdulagatov, Y. Yan, J.R. Cooper, Y. Zhang, Z.M. Gibbs, A.S. Cavanagh, R.G. Yang, Y.C. Lee, and S.M. George, ACS Appl. Mater. Interfaces **3**, 4593 (2011).

[10] V. Dokmai, R. Methaapanon, and V. Pavarajarn, Appl. Surf. Sci. **499**, 143906 (2020).

[11] G. Este and W.D. Westwood, J. Vac. Sci. Technol. A Vacuum, Surfaces, Film. **2**, 1238 (1984).

[12] C.P. Huang and W. Stumm, J. Colloid Interface Sci. **43**, 409 (1973).

[13] J.S.L. Leach and P. Neufeld, Corros. Sci. **9**, 413 (1969).

[14] G. Patermarakis, P. Lenas, C. Karavassilis, and G. Papayiannis, Electrochim. Acta **36**, 709 (1991).

[15] K. Tadanaga, N. Katata, and T. Minami, J. Am. Ceram. Soc. **80**, 3213 (2005).

[16] Z. Liu, J. Deng, and D. Li, Anal. Chim. Acta **407**, 87 (2000).

[17] Q. Chen, G. Hubbard, P.A. Shields, C. Liu, D.W.E. Allsopp, W.N. Wang, and S. Abbott, Appl. Phys. Lett. **94**, 263118 (2009).

[18] J. Tommila, A. Aho, A. Tukiainen, V. Polojärvi, J. Salmi, T. Niemi, and M. Guina, Prog. Photovoltaics Res. Appl. **21**, 1158 (2013).

[19] K.-S. Han, J.-H. Shin, W.-Y. Yoon, and H. Lee, Sol. Energy Mater. Sol. Cells **95**, 288 (2011).

[20] C.-H. Sun, B.J. Ho, B. Jiang, and P. Jiang, Opt. Lett. **33**, 2224 (2008).

[21] W.-L. Min, A.P. Betancourt, P. Jiang, and B. Jiang, Appl. Phys. Lett. **92**, 141109 (2008).

[22] H.-L. Chen, A. Cattoni, R. De Lépinau, A.W. Walker, O. Höhn, D. Lackner, G. Siefer, M. Faustini, N. Vandamme, J. Goffard, B. Behaghel, C. Dupuis, N. Bardou, F. Dimroth, and S. Collin, Nat. Energy **4**, 761 (2019).

[23] E.E. Perl, W.E. McMahon, J.E. Bowers, and D.J. Friedman, Opt. Express **22**, A1243 (2014).

[24] M. Keshavarz Hedayati and M. Elbahri, Materials (Basel). **9**, 497 (2016).

[25] C. Kauppinen, K. Isakov, and M. Sopanen, ACS Appl. Mater. Interfaces **9**, 15038 (2017).

[26] D.J. Friedman, Curr. Opin. Solid State Mater. Sci. **14**, 131 (2010).

[27] W. Weinstein, J. Opt. Soc. Am. **37**, 576 (1947).

[28] F. Abelès, Ann. Phys. (Paris). **12**, 596 (1950).

[29] A. Herpin, Comptes Rendus 182 (1947).

[30] M. Morita, T. Ohmi, E. Hasegawa, M. Kawakami, and M. Ohwada, J. Appl. Phys. **68**, 1272 (1990).

[31] I. Horcas, R. Fernández, J.M. Gómez-Rodríguez, J. Colchero, J. Gómez-Herrero, and A.M. Baro, Rev. Sci. Instrum. **78**, 1 (2007).

[32] D.E. Aspnes, Thin Solid Films **89**, 249 (1982).

[33] V.A. Markel, J. Opt. Soc. Am. A **33**, 1244 (2016).

[34] G.C. Correa, B. Bao, and N.C. Strandwitz, ACS Appl. Mater. Interfaces **7**, 14816 (2015).

[35] K. Wefers and C. Misra, Alcoa Tech. Pap. **19**, 1 (1987).

[36] G. Lefèvre, M. Duc, P. Lepeut, R. Caplain, and M. Fédoroff, Langmuir **18**, 7530 (2002).

[37] R. Schoen and C.E. Roberson, Am. Mineral. **55**, 43 (1970).

[38] M.L.P. Antunes, H.D.S. Santos, and P.D.S. Santos, Mater. Chem. Phys. **76**, 243 (2002).

[39] K. Isakov, C. Kauppinen, S. Franssila, and H. Lipsanen, ACS Appl. Mater. Interfaces **12**, 49957 (2020).

[40] R. King, C. Fetzer, D. Law, K. Edmondson, H. Yoon, G. Kinsey, D. Krut, J. Ermer, P. Hebert,

B. Cavicchi, and N. Karam, in *2006 IEEE 4th World Conf. Photovolt. Energy Conf.* (IEEE, 2006), pp. 1757–1762.

[41] S. Vaid, M. Kats, G. Hering, P. Blumenfeld, D. Buie, J. Nagyvary, J. Foresi, and P.A. Zawadzki, (2009).

[42] R.R. King, D.C. Law, K.M. Edmondson, C.M. Fetzer, G.S. Kinsey, H. Yoon, R.A. Sherif, and N.H. Karam, Appl. Phys. Lett. **90**, (2007).

[43] M. Wiemer, V. Sabnis, and H. Yuen, in *High Low Conc. Syst. Sol. Electr. Appl. VI*, edited by K. VanSant and R.A. Sherif (2011), p. 810804.

[44] J. Tommila, A. Aho, A. Tukiainen, V. Polojärvi, J. Salmi, T. Niemi, and M. Guina, Prog. Photovoltaics Res. Appl. **21**, 1158 (2013).

Appendix A.

Deposition parameters

IBS	Al_2O_3	SiO_2	TiO_2	Ta_2O_5
Target	Al purity of 99.999 %	Si purity of 99.999 %	Ti purity of 99.8 %	Ta purity of 99.95 %
Sputtering gas	$Ar:O_2$ (8:5 sccm)	$Ar:O_2$ (8:5 sccm)	$Ar:O_2$ (8:5 sccm)	$Ar:O_2$ (8:5 sccm)
Process gas [O_2] flow [sccm]	80	90	80	80
Deposition pressure [mbar]	4.5×10^{-4}	4.5×10^{-4}	4.5×10^{-4}	4.5×10^{-4}
RF power [W]	102	115	150	145
Sputtering Voltage [kV]	1.26	1.50	2.00	2.00

E-beam	Al_2O_3	SiO_2	TiO_2	Ta_2O_5
Target	Al_2O_3 purity of 99.999 %	SiO_2 purity of 99.99 %	TiO_2 purity of 99.9 %	Ta_2O_5 purity of 99.95 %
Additional O_2	no	no	yes	yes
Deposition pressure [mbar]	6×10^{-5}	5×10^{-5}	1.9×10^{-4}	1.5×10^{-4}
Substrate temperature [°C]	150	100	100	100

Appendix B.

Rugate models for DIW treated Al_2O_3

	E-beam	Start Design	Fitted	IBS	Start Design	Fitted
Layer Nbr	**Refractive Index**	**Physical Thickness [nm]**	**Physical Thickness [nm]**	**Refractive Index**	**Physical Thickness [nm]**	**Physical Thickness [nm]**
100	1.000	1.58	0.56	1.000	1.58	3.63
99	1.006	1.57	0.67	1.007	1.57	1.03
98	1.012	1.56	0.17	1.014	1.56	2.85
97	1.018	1.56	0.11	1.020	1.55	1.95
96	1.024	1.55	0.00	1.027	1.54	5.36

95	1.030	1.54	2.97	1.034	1.53	2.22
94	1.036	1.53	0.01	1.041	1.52	5.10
93	1.042	1.52	3.57	1.047	1.51	13.07
92	1.048	1.51	1.77	1.054	1.50	10.95
91	1.053	1.50	0.05	1.061	1.49	11.96
90	1.059	1.49	0.01	1.068	1.48	20.41
89	1.065	1.49	0.59	1.074	1.47	5.93
88	1.071	1.48	5.28	1.081	1.47	21.55
87	1.077	1.47	32.32	1.088	1.46	1.87
86	1.083	1.46	10.37	1.095	1.45	0.73
85	1.089	1.45	7.65	1.101	1.44	0.48
84	1.095	1.45	19.29	1.108	1.43	0.35
83	1.101	1.44	4.54	1.115	1.42	1.63
82	1.107	1.43	0.36	1.122	1.41	2.85
81	1.113	1.42	7.13	1.128	1.40	3.08
80	1.119	1.42	4.26	1.135	1.40	3.42
79	1.125	1.41	1.95	1.142	1.39	0.88
78	1.131	1.40	0.40	1.149	1.38	0.11
77	1.137	1.39	0.40	1.155	1.37	3.31
76	1.143	1.39	2.91	1.162	1.36	5.36
75	1.149	1.38	0.26	1.169	1.36	4.95
74	1.155	1.37	0.02	1.176	1.35	18.71
73	1.160	1.37	0.06	1.182	1.34	21.03
72	1.166	1.36	0.01	1.189	1.33	14.06
71	1.172	1.35	0.56	1.196	1.33	0.34
70	1.178	1.35	0.01	1.203	1.32	1.44
69	1.184	1.34	0.01	1.209	1.31	1.87
68	1.190	1.33	0.15	1.216	1.30	8.00
67	1.196	1.33	0.18	1.223	1.30	3.28
66	1.202	1.32	0.06	1.230	1.29	2.11
65	1.208	1.31	0.30	1.236	1.28	1.29
64	1.214	1.31	0.00	1.243	1.28	0.61
63	1.220	1.30	0.02	1.250	1.27	0.88
62	1.226	1.29	0.14	1.257	1.26	1.40
61	1.232	1.29	0.09	1.263	1.26	0.73
60	1.238	1.28	0.04	1.270	1.25	0.74
59	1.244	1.28	0.03	1.277	1.24	0.44
58	1.250	1.27	0.01	1.284	1.24	0.55
57	1.256	1.26	0.01	1.290	1.23	0.40
56	1.262	1.26	0.00	1.297	1.22	0.42
55	1.267	1.25	0.02	1.304	1.22	0.36
54	1.273	1.25	0.59	1.311	1.21	0.71
53	1.279	1.24	0.45	1.317	1.21	0.88

52	1.285	1.23	0.50	1.324	1.20	0.79
51	1.291	1.23	0.01	1.331	1.19	0.48
50	1.297	1.22	0.18	1.338	1.19	1.02
49	1.303	1.22	0.30	1.344	1.18	0.90
48	1.309	1.21	0.01	1.351	1.18	0.64
47	1.315	1.21	0.16	1.358	1.17	0.06
46	1.321	1.20	0.29	1.365	1.16	0.03
45	1.327	1.20	0.31	1.371	1.16	0.06
44	1.333	1.19	0.02	1.378	1.15	0.01
43	1.339	1.19	0.03	1.385	1.15	0.01
42	1.345	1.18	0.08	1.392	1.14	0.07
41	1.351	1.18	0.46	1.398	1.14	0.24
40	1.357	1.17	0.17	1.405	1.13	0.10
39	1.363	1.17	0.00	1.412	1.13	0.19
38	1.369	1.16	0.63	1.419	1.12	0.21
37	1.374	1.16	0.75	1.426	1.11	0.02
36	1.380	1.15	1.07	1.432	1.11	0.09
35	1.386	1.15	0.92	1.439	1.10	0.15
34	1.392	1.14	0.15	1.446	1.10	0.07
33	1.398	1.14	0.02	1.453	1.09	0.26
32	1.404	1.13	0.08	1.459	1.09	0.00
31	1.410	1.13	0.08	1.466	1.08	0.07
30	1.416	1.12	0.20	1.473	1.08	0.05
29	1.422	1.12	0.23	1.480	1.07	0.02
28	1.428	1.11	0.03	1.486	1.07	0.10
27	1.434	1.11	0.01	1.493	1.06	0.01
26	1.440	1.10	0.13	1.500	1.06	0.01
25	1.446	1.10	0.17	1.507	1.06	0.02
24	1.452	1.09	0.15	1.513	1.05	0.05
23	1.458	1.09	0.13	1.520	1.05	0.02
22	1.464	1.09	0.07	1.527	1.04	0.03
21	1.470	1.08	0.11	1.534	1.04	0.09
20	1.475	1.08	0.11	1.540	1.03	0.01
19	1.481	1.07	0.11	1.547	1.03	0.14
18	1.487	1.07	0.01	1.554	1.02	0.01
17	1.493	1.06	0.05	1.561	1.02	0.06
16	1.499	1.06	0.30	1.567	1.01	0.03
15	1.505	1.06	0.11	1.574	1.01	0.00
14	1.511	1.05	0.25	1.581	1.01	0.01
13	1.517	1.05	0.00	1.588	1.00	0.01
12	1.523	1.04	0.00	1.594	1.00	0.40
11	1.529	1.04	0.00	1.601	0.99	0.02
10	1.535	1.04	0.05	1.608	0.99	0.02

9	1.541	1.03	0.08	1.615	0.99	0.00
8	1.547	1.03	0.53	1.621	0.98	0.00
7	1.553	1.02	0.96	1.628	0.98	0.08
6	1.559	1.02	0.28	1.635	0.97	0.10
5	1.565	1.02	1.16	1.642	0.97	0.30
4	1.571	1.01	0.01	1.648	0.97	0.15
3	1.577	1.01	0.47	1.655	0.96	0.07
2	1.582	1.01	0.85	1.662	0.96	0.26
1	1.588	1.00	2.09	1.669	0.95	0.34